

Nonlinear instabilities of TPMS cellular units under axially loaded conditions

Fu, Hao; Huang, Xu; Kaewunruen, Sakdirat

DOI:

[10.1142/S0219455424502614](https://doi.org/10.1142/S0219455424502614)

License:

Creative Commons: Attribution (CC BY)

Document Version

Peer reviewed version

Citation for published version (Harvard):

Fu, H, Huang, X & Kaewunruen, S 2024, 'Nonlinear instabilities of TPMS cellular units under axially loaded conditions', *International Journal of Structural Stability and Dynamics*.

<https://doi.org/10.1142/S0219455424502614>

[Link to publication on Research at Birmingham portal](#)

General rights

Unless a licence is specified above, all rights (including copyright and moral rights) in this document are retained by the authors and/or the copyright holders. The express permission of the copyright holder must be obtained for any use of this material other than for purposes permitted by law.

- Users may freely distribute the URL that is used to identify this publication.
- Users may download and/or print one copy of the publication from the University of Birmingham research portal for the purpose of private study or non-commercial research.
- User may use extracts from the document in line with the concept of 'fair dealing' under the Copyright, Designs and Patents Act 1988 (?)
- Users may not further distribute the material nor use it for the purposes of commercial gain.

Where a licence is displayed above, please note the terms and conditions of the licence govern your use of this document.

When citing, please reference the published version.

Take down policy

While the University of Birmingham exercises care and attention in making items available there are rare occasions when an item has been uploaded in error or has been deemed to be commercially or otherwise sensitive.

If you believe that this is the case for this document, please contact UBIRA@lists.bham.ac.uk providing details and we will remove access to the work immediately and investigate.

Nonlinear instabilities of TPMS cellular units under axially loaded conditions

Hao Fu, Xu Huang and Sakdirat Kaewunruen*

Laboratory for Track Engineering and Operations for Future Uncertainties (TOFU Lab), Department of Civil Engineering, School of Engineering, The University of Birmingham, Edgbaston, B15 2TT, Birmingham, United Kingdom; S.Kaewunruen@bham.ac.uk

Received Day Month Year

Revised Day Month Year

In recent years, significant research has been conducted to explore the use of 3D triply periodic minimal surface (TPMS) structures for their exceptional vibrational damping properties and their ability to provide a continuous, smooth surface. The emergence of 3D printing has enabled the application of TPMS structures in fields such as medicine and aviation. In civil engineering, the compressive capacity of structures is a fundamental parameter in structural design. To evaluate the potential of porous TPMS structures in civil engineering, we have designed and manufactured four types of Skeletal-TPMS units using Stereolithography (SLA) technology. Axially loaded tests and nonlinear finite element method (NFEM) simulations have been performed to investigate the compressive strength and stiffness of the units. Our findings indicate that compared to solid blocks, the compressive strength of Skeletal-TPMS units decreases by 71.3% to 82.6%, and the stiffness decreases by 64.9% to 79.2%. The Skeletal-SP units show better compressive resistance than Skeletal-IWP units. This study provides new valuable insights for structural design and applications using TPMS structures in civil engineering.

Keywords: Triply periodic minimal surface (TPMS); Instability; Failure mode; Finite element analysis (FEM); Stereolithography; Compressive strength; Stiffness.

1. Introduction

Cellular structures are porous and lightweight structures that comprise periodically or randomly distributed cellular units¹. These structures are naturally occurring in the organs of plants and animals²⁻⁴, which has prompted numerous researchers to investigate their properties⁵⁻⁹. Studies have demonstrated that cellular structures exhibit excellent energy absorption capacity, high stiffness-to-weight ratios, and good thermal conductivity. The mechanical properties of cellular structures are influenced by various factors, including the material properties, manufacturing process, cellular unit geometry, and arrangement of units^{6, 10-14}. With the development of 3D printing technology, various cellular structures with low density and high damping properties can now be fabricated and utilized in many fields. Cellular structures can be categorized into three main types based on the closure property of the cellular units: open-cell, hybrid-cell, and closed-cell structures. Researchers also named cellular structures from the shape and structural form of the cellular unit, such as honeycomb sandwich structure^{15, 16}, Auxetic-strut¹⁷, foamed aluminum, lattice

* Corresponding author.

structure^{18, 19}, Sheetal triply periodic minimal surface (TPMS) structure¹¹, Skeletal TPMS structure²⁰, among others.

TPMS structures are a novel type of intelligent porous structure. Typically, TPMS structures can be built by thickening a particular TPMS or by closing the open holes of a TPMS. The employment of TPMSs confers a multitude of advantages; notably, they exhibit continuous zero mean curvature and unbroken interlinking channels. Moreover, the crystalline framework of structures predicated on TPMS, originating from the tridimensional periodic symmetrical assemblies, provides a considerable boon in terms of mechanical characteristics. The advancement of additive manufacturing and numerical simulation technologies over the past two decades has heightened the researchers' interest in the properties of TPMS structures. Notably, Eric A. Lord²¹ investigated seven families of TPMS and 24 TPMS using Surface Evolver, revealing that the topology of TPMS is characterized by two interpenetrating networks. Additionally, S. Torquato²² studied the shear resistance of Schwartz-P (SP) and D surfaces, finding that these two TPMSs exhibit similar shear stiffness. Diab W. Abueidda¹¹ designed, manufactured, and tested Sheetal SP, IWP, and Neovius TPMS structures of 23.5% relative density. Their research indicated that Sheetal IWP structures possess double compressive strength and better energy absorption properties compared to Sheetal SP structures. Similarly, Oraib Al-Ketan²⁰ investigated the compressive strength of five types of Skeletal TPMS structures with various relative densities, revealing that the secondary IWP structure has the highest compressive strength and Young's stiffness among all the TPMS structures. The main deformation mode of Skeletal TPMS structures is bending-dominated, making them ideal for energy-absorbing and damage-tolerance applications. Oraib Al-Ketan²³ further evaluated the compressive behaviors of strut-based structures, Skeletal TPMS structures, and Sheetal TPMS structures manufactured from maraging steel. Their research revealed that Sheetal TPMS structures exhibit near stretching-dominated deformation behavior while Skeletal TPMS structures have bending-dominated behavior. The Skeletal Gyroid structures manufactured from verowhite and tangogray were also tested by Oraib Al-Ketan²⁴. In addition, I. Maskerya²⁵ tested and simulated Skeletal Gyroid, Skeletal-Diamond, and Skeletal SP TPMS structures, with results showing that the Skeletal-primitive TPMS structure has the highest compressive strength among all types of structures. Lei Zhang²⁶ conducted similar research on metallic Sheet-TPMS structures with SP, Diamond, and Gyroid surfaces using compressive tests and FEM simulations. Their findings indicated that Sheetal TPMS structures outperform lattice structures in terms of surface area, damping properties, and compressive behavior. Similarly, Diab W. Abueidda²⁷ evaluated the mechanical properties of structures with Gyroid, SP, IWP, and Neovius TPMS sheet units, with results showing that the TPMS structures with Neovius and IWP sheet units have the greatest compressive strength and energy-absorbing capability. Oraib Al-Ketan²⁸ concluded that CLP Sheetal TPMS structures outperform Gyroid Sheetal TPMS structures and Schwartz P Sheet-TPMS structures in compressive properties as well as stress distribution. In contrast, Minhao Shen¹¹ reported that the order of compressive strength was S14 > IWP > Gyroid > SP, based on compressive tests. Hanfeng Yin²⁹ established four types of Sheetal TPMS

structures based on Schwartz P, IWP, FRD, and Gyroid and investigated their energy-absorbing capacity using FEM software LS-DYNA. Their research indicated that the structures with Sheetal IWP units and Sheetal FRD units have higher compressive strength than other Sheetal TPMS structures. Weimin Jiang³⁰ built several solid lock hinges with TPMS structures.

Prior studies have shown that both Sheetal and Skeletal TPMS structures exhibit superior energy absorption compared to conventional structures like honeycombs and foamed aluminums. However, a consensus on the most efficient structure is still unclear. TPMS units, typically ranging from 0.1 to 7 millimeters, are used in biomedical applications^{10, 11, 23-29, 31-37}, but are less suitable for civil engineering due to size constraints. Skeletal TPMS structures seem to offer a more practical approach for civil applications. Recent focus has been on Sheet TPMS structures, while Skeletal TPMS structures remain underexplored. Despite their potential that Skeletal TPMS could significantly impact areas like vibration reduction and energy absorption^{38, 39}, Skeletal TPMS structures are rarely investigated in civil engineering. The advancement of additive manufacturing suggests TPMS structures could be revolutionary in civil engineering, especially in dynamic load environments like railways⁴⁰ or earthquake-prone areas^{41, 42}. However, the properties of large-sized TPMS units remain unexplored, highlighting the need for further research. This study investigates potential nonlinear instabilities in single large-sized Skeletal-TPMS units under compressive loads, utilizing two TPMS types, SP and IWP, produced via SLA 3D printing. Compressive tests on cube blocks and Skeletal TPMS samples, supported by FEM models, reveal vital insights. Our findings address a research gap, emphasizing safety and identifying nonlinear instabilities, and offer valuable contributions for advancing porous TPMS structures in civil and railway engineering, enhancing our understanding of their mechanical properties and potential applications.

2. Geometry, manufacturing and material

Since the discovery and description of the first TPMS by Schwarz in 1865⁴³, numerous TPMSs have been proposed by researchers^{21, 44, 45}. However, many TPMSs are non-uniformly distributed in space or non-symmetric in three axes as shown in Figure 1. In civil engineering fields, it is crucial to choose TPMS with bicontinuous cubic microdomain morphologies through symmetries to ensure uniform force distribution in space. The SP surface and the IWP surface, both symmetrical, have solid skeletons formed by closing their open holes, which possess good connectivity. Additionally, these two TPMS structures were found to have excellent damping properties^{44, 46}. Therefore, the SP surface and the IWP surface were chosen to build cellular units.

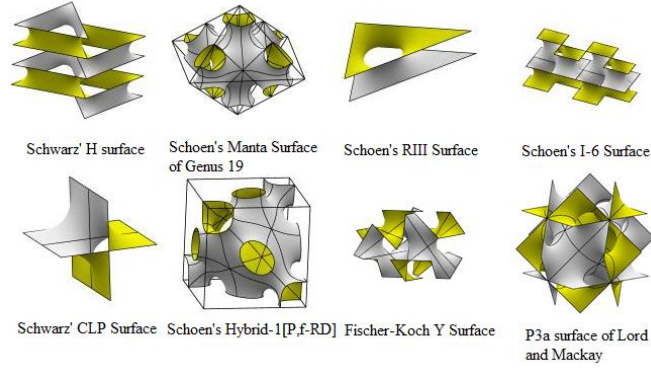


Figure 1. Diagram of various types of TPMS.

TPMS structure is a mathematically defined surface with unique characteristics such as three-dimensional (3D) periodicity, zero average curvature, and a large surface area. These properties allow the TPMS to divide space into two sub-domains while maintaining open space, making them an attractive option for various applications and prompting researchers to explore their features. Specifically, TPMS surfaces are defined by a set of mathematical equations, and can be described generally by the following formula^{29, 47}, while the approximations of the Schwarz Primitive (SP) can be defined using Eq. 2.2^{23, 48, 49} and the nodal approximation of the IWP surface is Eq. 2.3^{32, 48}.

$$\phi(r) = \sum_{k=1}^K A_k \cos \left[\frac{2\pi(h_k \cdot r)}{\lambda_k} + p_k \right] = C \quad (2.1)$$

$$\phi(r) = \cos\left(\frac{2\pi x}{l}\right) + \cos\left(\frac{2\pi y}{l}\right) + \cos\left(\frac{2\pi z}{l}\right) = C \quad (2.2)$$

$$\phi(r) = 2\left[\cos\left(\frac{2\pi x}{l}\right)\cos\left(\frac{2\pi y}{l}\right) + \cos\left(\frac{2\pi y}{l}\right)\cos\left(\frac{2\pi z}{l}\right) + \cos\left(\frac{2\pi z}{l}\right)\cos\left(\frac{2\pi x}{l}\right)\right] - \left[\cos\left(\frac{2\pi \cdot 2x}{l}\right) + \cos\left(\frac{2\pi \cdot 2y}{l}\right) + \cos\left(\frac{2\pi \cdot 2z}{l}\right)\right] = C \quad (2.3)$$

where r is the position vector in the three-dimensional Euclidean space, A_k is the amplitude factor, h_k is the lattice vector in the reciprocal space, λ_k is the wavelength of periods, p_k is the phase shift, C represents a constant known as the level set. Among those parameters, A_k and h_k have the greatest influence on the geometric shape of the 3D surface, and C determines whether the surface is the minimal surface. It should be noted that the geometry is no longer a minimal surface if the constant C does not equal zero⁴⁸. In Eq. 2.2 and 2.3, x, y and z represent three Cartesian coordinates and l denotes the length of the unit.

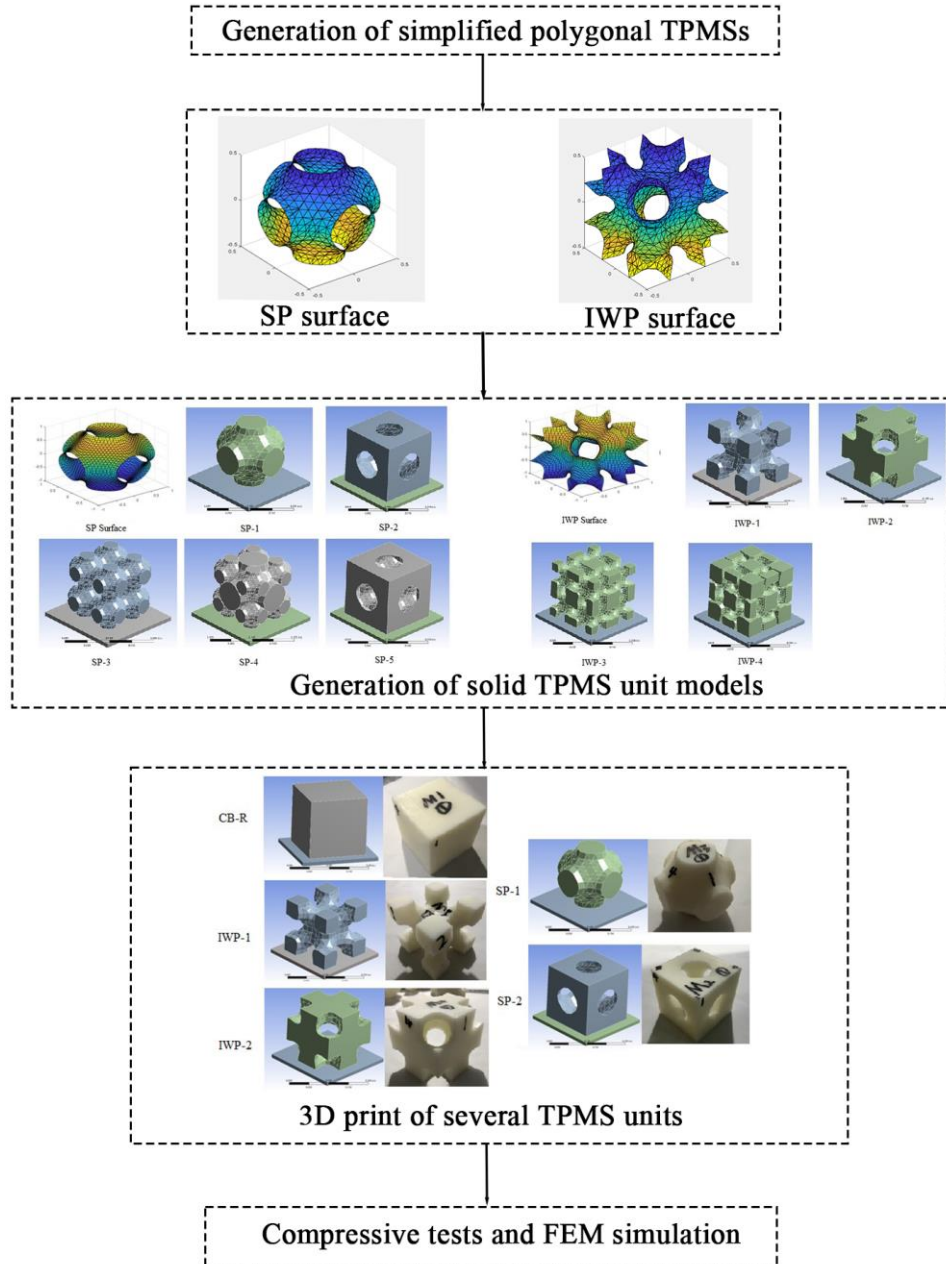


Figure 2. Flow chart diagram depicting the generation of TPMS units.

Figure 2 depicts the procedures for generating the TPMS units currently examined in this research. Initially, through the application of nodal approximation equations for SP

and IWP, a custom-developed Matlab script is employed to transform continuous TPMS surfaces into polygonal surfaces, consisting of multiple triangular facets. This transformation includes exporting the simplified surface data, comprising nodes and meshes, into STL files. The purpose of this simplification is to reduce errors in subsequent 3D printing endeavours and to diminish the mesh quantity in Finite Element Method (FEM) simulations, thus accelerating computational efficiency. Subsequently, the SP and IWP surfaces, now simplified and encapsulated in STL files, are processed with Geomagic Studio software to seal their apertures, resulting in the SP-1 and IWP-1 units. The SP-2 and IWP-2 configurations are the complementary counterparts to SP-1 and IWP-1, respectively. Conversely, SP-3 and IWP-3 result from a reduction of the unit size by half and a subsequent layering. The type-4 structures, SP-4 and IWP-4, are composites of Type-III (SP-3 and IWP-3) and type-1 (SP-1 and IWP-1) structures. SP-5 amalgamates the attributes of SP-3 and SP-2. The comprehensive delineation of all generated SP and IWP structures is presented in Figure 2 under 'Generation of solid TPMS unit models'. Additionally, the relative densities and surface area ratios of all SP and IWP units, in comparison to cubic blocks, are listed in Table 1.

Table 1. Comparison of relative density and surface area between SP and IWP units and cube block

Unit type	Relative density	Surface area ratio (compared to CB-R)
CB-R	1.00	1.00
SP-1	0.50	0.57
SP-2	0.50	1.22
SP-3	0.50	0.97
SP-4	0.75	0.88
IWP-1	0.53	0.97
IWP-2	0.47	1.24
IWP-3	0.53	1.58
IWP-4	0.77	1.64

To facilitate subsequent compression testing and FEM simulations, five types of samples are fabricated, including the cube block for reference (CB-R), IWP-1, IWP-2, SP-1, and SP-2. The 3D printing is conducted by WeNext, a prominent Chinese 3D printing firm, employing the Stereolithography (SLA) technique. All specimens are constructed from photosensitive resin 8200, a composite material imbued with additives supplied by Royal DSM Inc. The density of this photosensitive resin 8200 has been measured as $\rho_s=1160 \text{ kg/m}^3$. Its mechanical properties have been ascertained by Royal DSM Inc. in adherence to ASTM standards. For the ensuing finite element simulations, the material properties are set to the average values delineated in Table 2. The dimensions for each structure are uniform, at $5 \text{ cm} \times 5 \text{ cm} \times 5 \text{ cm}$. The precision of the SLA printing process has been ascertained at 0.1mm. Examples of the printed samples are shown in Figure 2 under '3D print of several TPMS units'.

Table 2. Mechanical properties of the photosensitive resin 8200 after curing.

Properties, unite	Test method	Value
-------------------	-------------	-------

Hardness, Shore D	ASTM D 2240	76~88
Flexural modulus, MPa	ASTM D 790	2692~2775
Flexural strength, MPa	ASTM D 790	69~74
Tensile modulus, MPa	ASTM D 638	2589~2695
Tensile strength, MPa	ASTM D 638	38~56

3. Laboratory test

3.1. Axially loaded tests

The electro-hydraulic servo universal testing machine, as illustrated in Figure 3a, is used to carry out the compression tests. Prior to the test, the instrument is calibrated to ensure accuracy. During the compression tests, the samples are positioned in the center of the bearing plate to ensure even loading. To avoid the orientation of the 3D printing impacting the compressive tests, the orientation of the samples is kept the same as the 3D printing direction. Since the mechanical properties of the photosensitive resin material are affected by the strain rate⁵⁰, a fixed vertical velocity is set for the loading plate of the compressive test machine to maintain consistency across all tests. The machine's data acquisition system automatically records the displacement and loading force during the loading process with a displacement resolution of 0.01 mm and a force resolution of 0.01 kN. The load's strain rate is set at 0.001 per second and the velocity of the loading plate at 0.05 mm per second in accordance with the study⁵¹. The samples are loaded until failure, and each of the five types of 3D printed samples (i.e., the cube block (CB-R), IWP-1, IWP-2, SP-1, and SP-2) undergoes three compressive tests. The states of the samples under testing, before and after the compressive test, are displayed in Figure 3b.

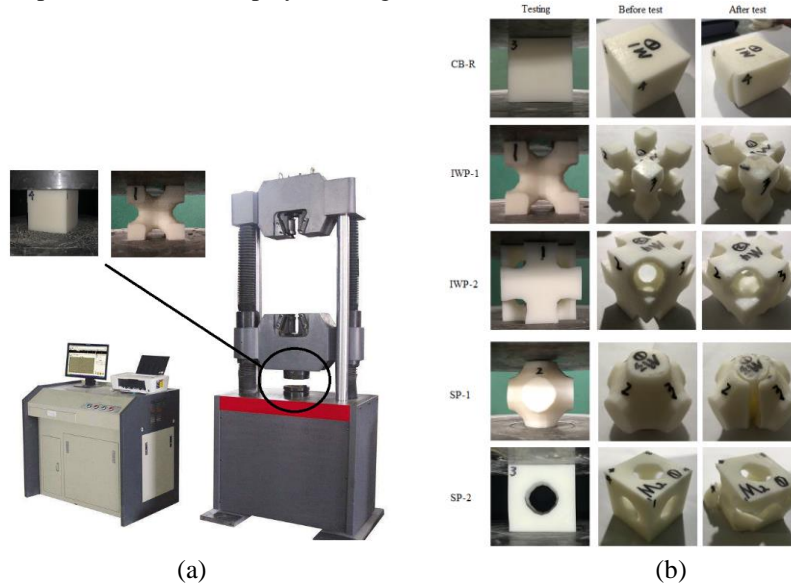


Figure 3. Axially loaded tests. (a) schematic of compressive tests and (b) sample states before, during and after the test.

3.2. Experimental results

3.2.1. Load-displacement curve

Each unit type undergoes three tests, and the average test results are calculated. The load-displacement curves of the tested units are illustrated in Figure 4a, while the load-displacement curves of the TPMS units are presented in Figure 4b to provide a clearer view of their trends. CB-R in the legends represents the reference group of cubic block sample, and TA represents the average value of the test results. The meaning of the other legends is similar to CB-R-TA. The slope of the curve indicates the stiffness of the unit. All other types of units except SP-1 exhibit a similar trend in the load-displacement curves. Generally, the load-displacement curves can be divided into three stages. In the first stage, the load increases approximately linearly as the displacement increases, reaching a displacement limit between 1.5-2.5 mm. In the second stage, the samples begin to yield, and the stiffness of the units tends to reduce from positive to negative at a certain point. As the displacement increases, the load rises to its peak value and then begins to decrease. After a small decrease in load, the curve becomes flat, and the stiffness of the structure approaches zero. Zhengning Li⁵² observed a similar trend of a cuboid sample manufactured from UV resin. With regard to the SP-1 structure, the first and third stages of the load-displacement curve are similar to those of other types of units. However, no negative part can be observed in the second stage. In this stage, the slope of the load-displacement gradually drops to zero. The difference between the SP-1 and other types of units can be attributed to their geometric differences near the area of the edges of their boundary box, causing different stress paths inside the tested samples. The TPMS units and the cube block yielded at a close vertical displacement.

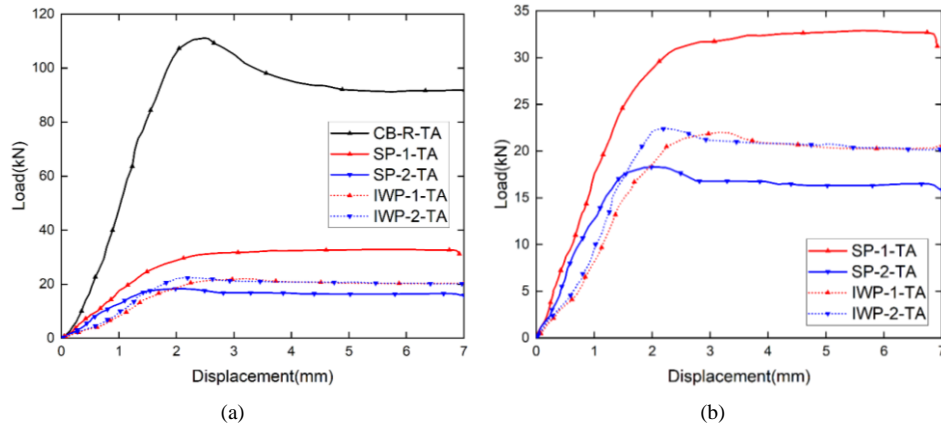


Figure 4. Load-displacement curves from compressive tests (a) the average load-displacement curves of all units and (b) the average load-displacement curves of TPMS units.

3.2.2. Compressive strength and secant stiffness

The compressive strength of each unit type is obtained by dividing the ultimate load by the cross-sectional area (50 mm × 50 mm) of the boundary box. As shown in Figure 5a. The CB-R unit exhibits the highest compressive strength among all TPMS-based units. In comparison, the compressive strength of IWP-1, IWP-2, SP-1, and SP-2 is reduced by 80.19%, 79.92%, 72.18%, and 83.55%, respectively, when compared to CB-R. As indicated in Table 1, the relative density of IWP-1, IWP-2, SP-1, and SP-2, relative to CB-R, is 0.53, 0.47, 0.5, and 0.5, respectively. The percentage decrease in the compressive strength of the TPMS units exceeds the percentage decrease in relative density. This phenomenon can be attributed to the stress transmission path inside the cube block being much shorter than in the TPMS units during compressive tests. As a result, many elements within the TPMS units do not fully exert their compressive performance in comparison to the cubic block. This could also explain the observation that the compressive strength of the SP-1 unit is 40.47%, 38.58%, and 69.08% higher than that of the SP-2 unit with the same density, and the IWP-1 and IWP-2 units with similar relative density, respectively. Moreover, the secant stiffness of the TPMS units is more than halved when compared to the cube block, as shown in Figure 5b. Among the four types of Skeletal-TPMS units tested, the SP-1 unit exhibits the highest secant stiffness and compressive strength. From a compressive performance perspective, the SP-1 unit outperforms other types of TPMS units tested.

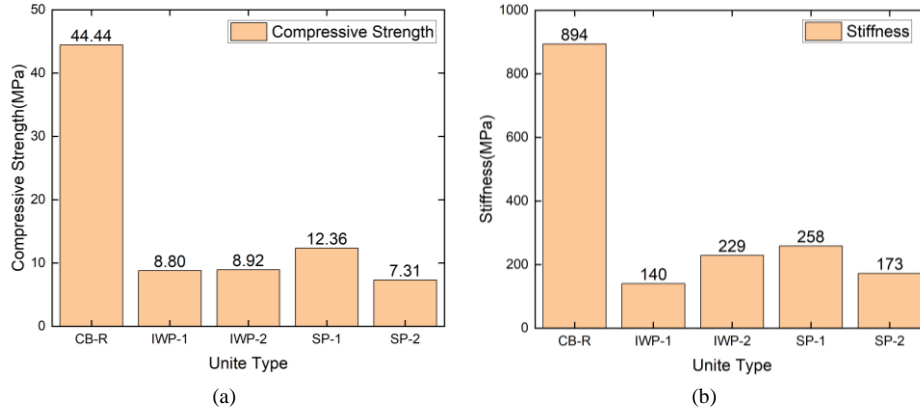


Figure 5. Test results of CB-R, IWP-1, IWP-2, SP-1 and SP-2 units. (a) compressive strength and (b) secant stiffness.

4. Numerical modeling

In this section, we employ the commercial FEM software Ansys to perform numerical analysis and simulate the compressive tests in order to compare the results with the corresponding experimental data. After validating the models based on the experimental results, we conduct further simulations and analyses for IWP-3, IWP-4, SP-3, SP-4, and SP-5 units.

4.1. FEM model

4.1.1. Model description

The FEM models are constructed with three parts, namely the loading plate, the test sample, and the bearing plate, as demonstrated in Figure 6. To ensure consistency with the compression tests, these three components are employed. Studies conducted by Ref.^{53, 54} suggest that the models can be simplified without significantly affecting the results due to the symmetry of TPMS units, load, and constraints. Therefore, to decrease simulation time, all FEM models are simplified to 1/4 of their original size. Symmetry constraints are enforced on the symmetry plane of the model. Based on trial calculations, the difference between the simulation results of the 1/4 models and the initial models is less than 0.1%. The loading plate and bearing plate in the 1/4 models have dimensions of 35 mm \times 35 mm \times 35 mm.

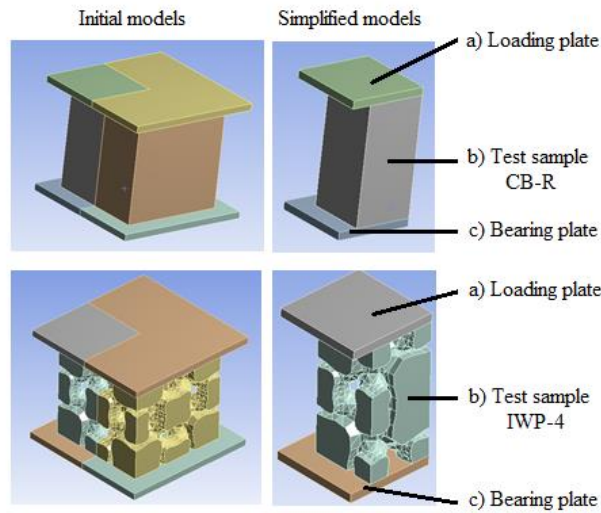


Figure 6. Schematic of FEM models of CB-R and IWP-4

4.1.2. Material properties

(i) loading plate and bearing plate

The loading plate and bearing plate are constructed of steel, therefore the structural steel material parameters in the ANSYS material library are chosen for simulating both plates, as outlined Table 3. The simulation does not account for the failure or yield of steel structures. The solid-186 elements are employed to simulate both plates, with the elastic constitutive model being utilized. The mesh size of the loading plate and bearing plate for all FEM simulations is set to 3.5 mm.

Table 3. General properties of the bearing plate and loading plate.

Properties	Value
Density	7.85g/cm ³
Young's modulus	200GPa
Poisson's ratio	0.3

(ii) CB-R and TPMS based units

The photosensitive resin is a polymer-based elastoplastic material. To consider non-identical material behavior, the Drucker-Prager plasticity model is employed as suggested in ⁵⁵. Material failure is simulated by utilizing the Drucker-Prager model together with a yield criterion. The material failure can be simulated by using the Drucker-Prager model together with a yield criterion. Dean and Wright⁵⁶ employed the linear Drucker-Prager plasticity model in numerical simulations of indentation tests conducted at various deformation velocities. Wenzhi Wang ⁵⁷ also adopted the Drucker-Prager constitutive model in Abaqus to simulate the 3D printed photosensitive resin. Both of their FEM results were in good agreement with experimental results. Therefore, all the TPMS units and the CB-R unit are modelled as a homogeneous elastoplastic material with a linear Drucker-Prager constitutive model.

In this model, several parameters need to be defined, including the plastic strain at uniaxial compressive strength, ultimate effective plastic strain in compression, relative stress at the onset of nonlinear hardening, residual compressive relative stress, plastic strain limit in tension, and residual tensile relative stress as shown in Figure 7 and Table 4. The κ axle denotes the plastic strain; the Ω_c denotes the ratio of compressive stress to uniaxial compressive strength; the Ω_t denotes the ratio of tensile stress to uniaxial tensile strength. The ductile failure with damage evolution is used as the failure criterion⁵⁸. The parameters shown in Table 4 are adopted in FEM simulation according to the material properties provided by WeNext Ltd and the data of the compressive tests. The solid-187 elements with ten nodes are used. A mesh sensitivity analysis is carried out for all Skeletal-TPMS units, ranging from 5 mm to 2 mm, and the results converge to a specific value as the mesh size decreases. A mesh size of 2 mm is therefore used for all Skeletal-TPMS units.

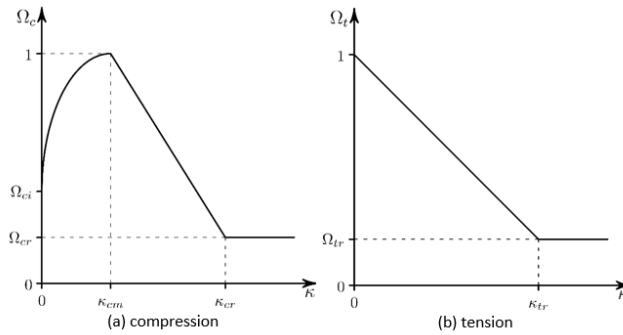


Figure 7. Linear Drucker-Prager constitutive model

Table 4. Properties of the TPMS FEM models

Properties	Value
------------	-------

Density	1.16g/cm ³
Young's modulus	2.6GPa
Poisson's ratio	0.42
Plastic strain at uniaxial compressive strength / κ_{cm}	0.04
Ultimate effective plastic strain in compression / κ_{cr}	0.13
Relative stress at onset of nonlinear hardening / Ω_{cl}	0.1
Residual compressive relative stress / Ω_{cr}	0.67
Plastic strain limit in tension / κ_{tr}	0.15
Residual tensile relative stress / Ω_{tr}	0.4

4.1.3. *Boundary conditions and loading process*

As illustrated in Figure 8, a standard gravitational acceleration is applied to all components in the FEM model, and the fixed boundary condition is imposed on the bottom surface of the bearing plate to mimic the actual compressive test scenario. A vertical displacement of 5 mm is prescribed on the loading plate with a simulation time of 100 s to match the experimental conditions. This configuration corresponds to a vertical velocity of 0.05 mm/s, resulting in a strain rate of 0.001/s, which is consistent with the strain rate used in the previous compression experiments.

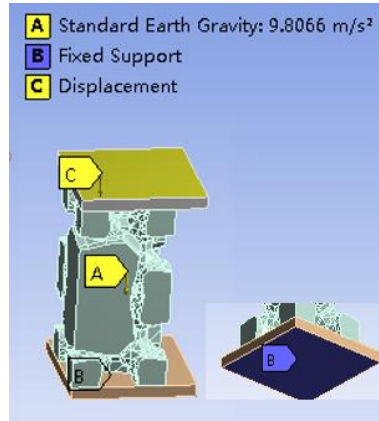


Figure 8. Boundary and loading conditions of FEM models

In order to ensure interaction and load transfers among components, general frictional contact is assigned to all contact areas. It should be noted that the value of friction can significantly affect the simulation results⁵⁹. For this reason, a friction coefficient of 0.2 is estimated based on the surface conditions of the test units and the steel plates.

4.2. *Validation of finite element models*

The load-displacement response of CB-R, SP-1, SP-2, IWP-1 and IWP-2 units under vertical loading is measured using Ansys, which was comparable with the results of corresponding compressive tests. This simulation is performed to give a reference for validating further FEM compressive simulation of SP-3, SP-4, SP-5, IWP-3 and IWP-4

TPMS units. Numerical and experimental results are compared in Figure 9a, 9b and 9c. In the following figures, the T presents test, the S presents simulation, and T1, T2 and T3 represent the first, the second, and the third compressive test, respectively. The loading-displacement curve of each type of TPMS unit and the CB-R unit under the vertical load has a similar trend in the displacement of the whole interval. The difference between the test and the simulation in ascending part is caused by the difference between the Drucker-Prager constitutive model and the real 3D printed material. The differences in ultimate load between the simulation and the average experimental results of CB-R, IWP-1, IWP-2, SP-1 and SP-2 units are 0.9%, 7.8%, 6.1%, 3.1% and 5.9%, respectively. This can be attributed to the difference between the idealized symmetry of FEM models and the non-rigorous symmetry of actual compressive tests. The difference of results between the FEM modelling and compressive tests is acceptable because the experimental margin of error is 5% to 10%. Thus, a set of the parameters adopted for the FEM simulation of the photosensitive resin is considered validated based on the comparison. These parameters are set for all simulations of the TPMS units.

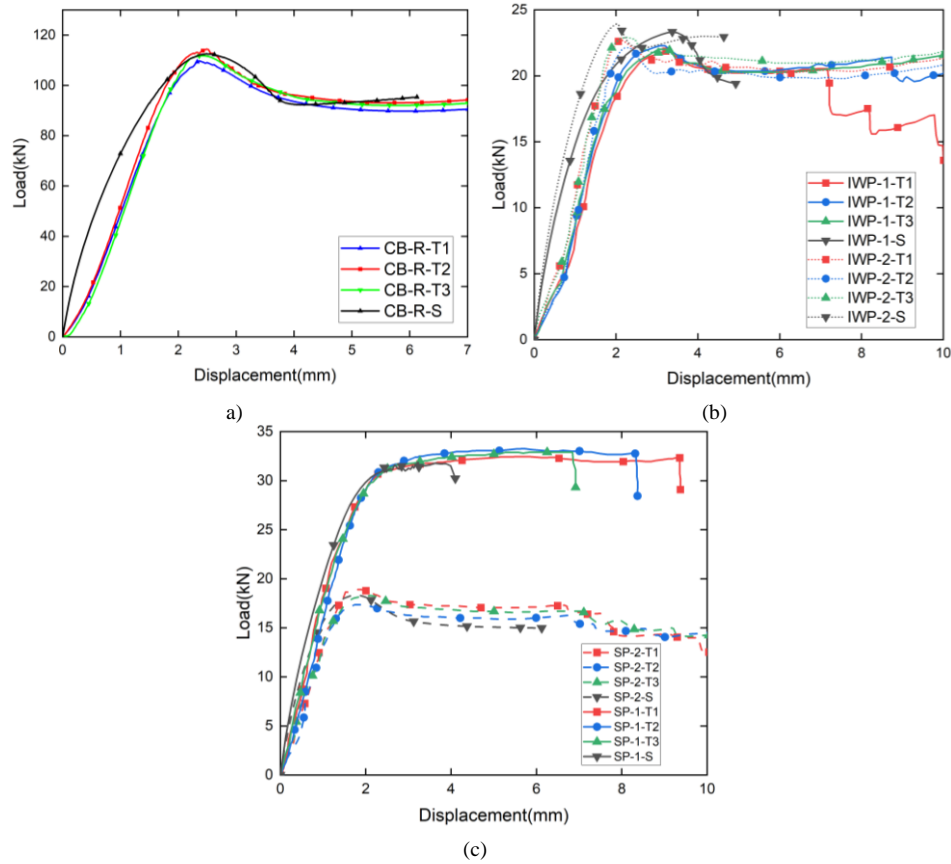


Figure 9. Comparison of load-displacement curves between FEM simulation and tests. (a) load-displacement curves of the CB-R unit from simulation and tests, (b) load-displacement curves of the IWP-1 and IWP-2 units

from simulation and tests and (c) load-displacement curves of the SP-1 and SP-2 units from simulation and tests.

4.3. FEM results

4.3.1. Load-displacement curve

Upon verification of the model, FEM is utilized to conduct compressive simulations on IWP-3, IWP-4, SP-3, SP-4, and SP-5 unit types. The load-displacement curves for all unit types are presented in Figure 10a and 10b. It is observed that all unit types exhibit a triphasic load-displacement behavior. During the first stage, the load increases linearly with displacement. In the second stage, the load growth rate decelerates and may even exhibit a decreasing trend. In the third stage, the stiffness of the unit structure approaches zero. At this stage, the TPMS structure may undergo large deformations, and the material may exhibit plasticity or instability, leading to potential nonlinear instabilities. Notably, the load-displacement curves of all TPMS units, except SP-1 and SP-4, present a descending segment in the second stage, with the plastic yield period occurring mainly at the displacement of 1.5-3mm. The value of displacement at the onset of the second stage is influenced by the type of unit structure, with a larger displacement value leading to a higher overall ultimate load for the structure. This suggests that TPMS units may exhibit plastic deformation or yield during this stage, which can lead to localized instabilities and deformations in the material.

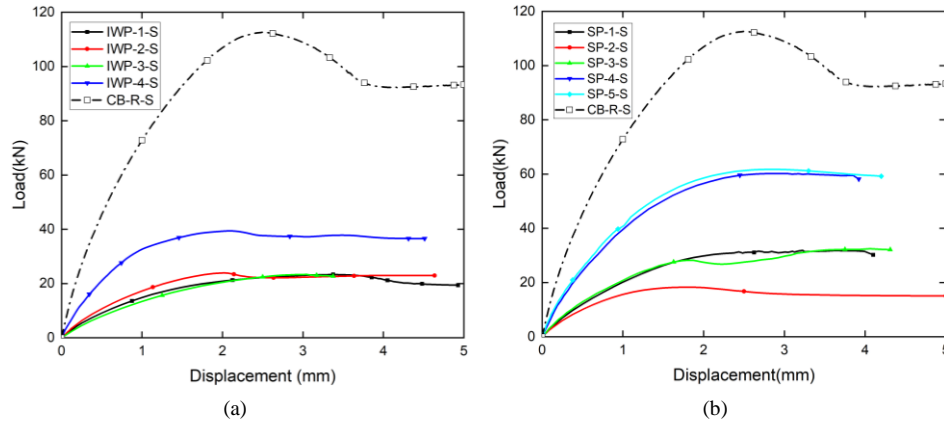


Figure 10. Load-displacement curves of all skeletal-TPMS units and CB-R unit from FEM simulation. (a) load-displacement curves of IWP based units and CB-R unit from FEM simulation and (b) load-displacement curves of SP based units and CB-R unit from FEM simulation

4.3.2. Compressive strength and secant stiffness

The ultimate load of the TPMS unit is determined by taking the peak load in the second stage of the load-displacement curve obtained from compression simulation. The compressive strength of the TPMS unit is then calculated by dividing the ultimate load by the cross-sectional area (50mm x 50mm). The approximate secant stiffness of the unit can

be obtained by dividing the compressive strength by the nominal strain at the peak load. Figure 11a shows that the compressive strength of all skeletal-TPMS units is lower than that of CB-R. Specifically, the strength of SP-based units is reduced by 58.9% to 83.7% compared to cube blocks, while the compressive strength of IWP-based units is reduced by 64.9% to 79.3%. The compressive strength of SP-3 is slightly lower than SP-1, while there is little difference in compressive strength between IWP-1 and IWP-3 units. These differences in compressive strength can be attributed to size effects and the interplay between the basic TPMS elements. Overall, the units in the SP groups exhibit higher compressive resistance when compared to those in the IWP group.

The secant stiffness of all unit types calculated from FEM analysis is listed in Figure 11b. Generally, units with higher compressive strength exhibit higher secant stiffness. To evaluate the compressive strength and secant stiffness, these values were divided by the relative density of the unit to the cube block. The specific compressive strength and compressive secant stiffness values are then calculated and presented in Table 6. Notably, SP-based units display superior compressive behavior than IWP-based units. Compressive resistance is a key parameter in civil engineering applications, and the findings suggest the superior potential of SP series units for such applications.

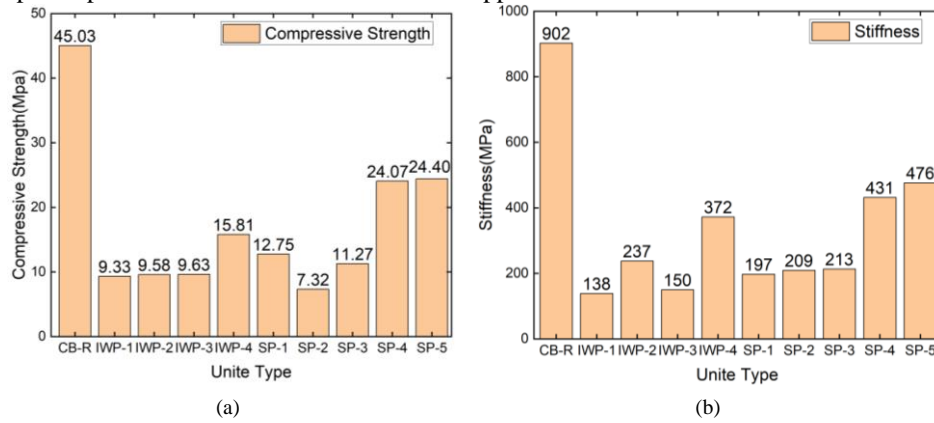


Figure 11. FEM results of all types of TPMS units. (a) compressive strength and (b) secant stiffness.

Table 5. FEM simulation results of different TPMS units.

Unit type	Compressive strength	Secant stiffness	Relative density to CBR	Compressive strength/RD	Secant stiffness /RD
CB-R	45.03	902	1	45.03	902
IWP-1	9.33	138	0.53	17.61	261
IWP-2	9.58	237	0.47	20.38	505
IWP-3	9.63	150	0.53	18.17	283
IWP-4	15.81	372	0.77	20.54	483
SP-1	12.75	197	0.5	25.50	395
SP-2	7.32	209	0.5	14.65	419
SP-3	11.27	213	0.5	22.55	426
SP-4	24.07	431	0.75	32.10	575
SP-5	24.40	476	0.75	24.40	635

4.3.3. Critical area

Figure 12 displays the equivalent stress distribution of all unit types at the peak load in the FEM simulation. Among the different TPMS units, IWP-2, SP-1 and SP-4 exhibit more areas where the equivalent stress approaches the maximum value, indicating that the compressive force from the top plate is more evenly distributed in these units. This may explain why these three units have higher compressive strength compared to other TPMS based units but may also lead to localized instabilities and deformations in the material. It should be noted that improving damping performance comes at the expense of reducing compressive capacity.

Furthermore, Figure 13 shows the stress concentration in the finite element analysis, which indicates the damaged areas of the tested units in compressive tests. This can cause structural instabilities and failures. This correlation also verifies the reliability of the finite element simulation. It was observed that the IWP-1 and SP-2 units fractured and lost their bearing capacity after cracking, while the SP-1 and IWP-2 units still held a continuous skeleton after failure. From a safety perspective, the SP-1 and IWP-2 units outperform the others.

In summary, the nonlinear instabilities of TPMS structures can include plastic deformation, stress concentration, and damage, which can lead to structural instabilities and failures. Therefore, it is crucial to design and analyze TPMS structures carefully to ensure their stability and safety. This insight is instrumental for digital twinning implementation for modern railway infrastructures⁵⁸.

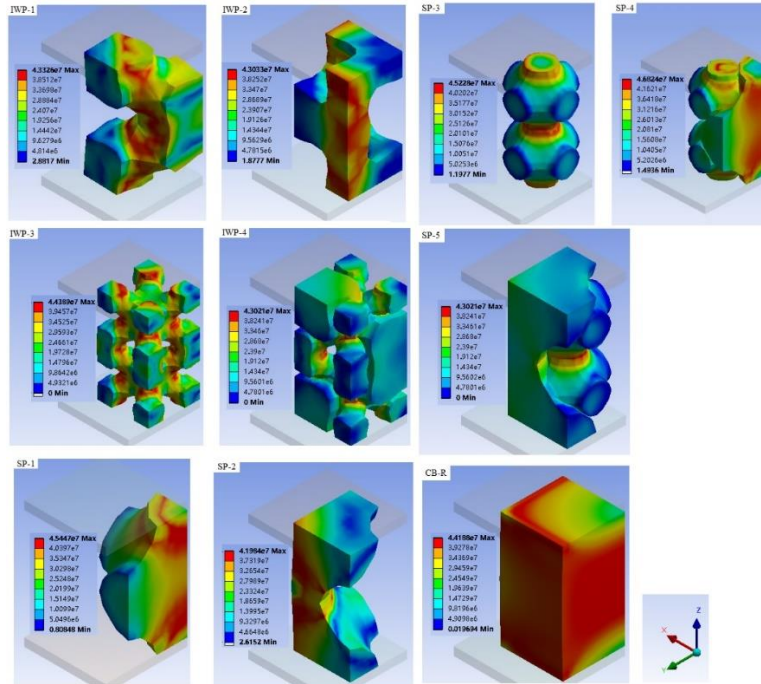


Figure 12. Distributions of the equivalent stress at the peak load for all types of units

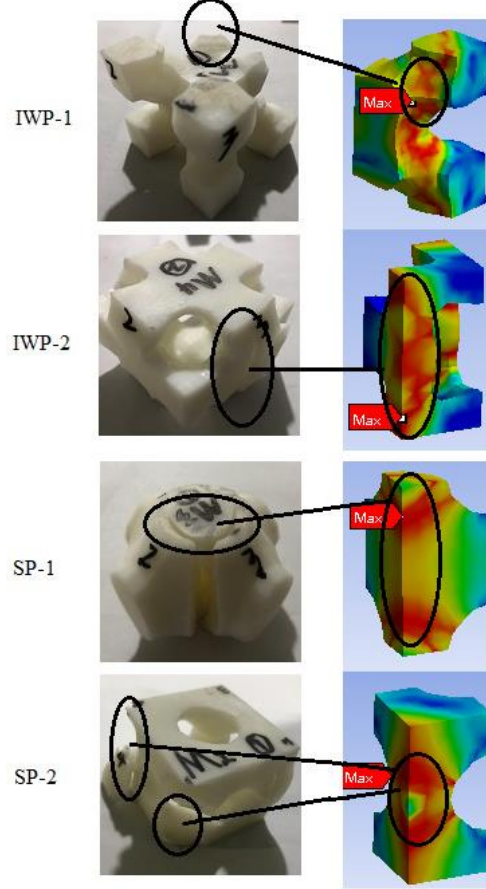


Figure 13. Comparison of critical areas between tests and FEM

5. Conclusions

Although excellent damping properties and energy-absorbing capacity characterize the TPMS structures, it is important to ensure that the smart porous structures have enough compressive capacity to bear loads in civil engineering fields. In this study, we have investigated the compressive properties and potential nonlinear instabilities of large-size single Skeletal-TPMS units for civil engineering applications, focusing on nine types of units based on IWP and SP surfaces. Through compressive tests, FEM simulations using the Drucker-Prager constitutive model, and the evaluation of five 3D printed samples, we have gained valuable insights into the compressive strength, secant stiffness, and nonlinear instabilities of these TPMS structures. The Drucker-Prager constitutive model, which we have employed in our FEM simulations, has allowed us to accurately reflect the softening behaviors of the 3D printed TPMS structures. This has been instrumental in providing a

more comprehensive understanding of their mechanical behavior under compression. Based on the results and discussion, the following conclusions are given.

1. The compressive strength and stiffness of the SP-based and IWP-based units decrease dramatically compared with the solid cube block. The high damping performance of TPMS structures comes at the expense of low compressive capacity. It is necessary to comprehensively consider energy absorption performance and strength and stiffness when a porous TPMS-based structure is utilized in civil engineering.
2. FEM simulation and results could illustrate the compressive behaviour of TPMS-based units and predict the critical areas inside a TPMS-based structure. In further designing of smart TPMS structures, the FEM can assist the designing procedure and predict damage.
3. Compared with IWP-based units, SP-based units show better compressive performance, including stiffness and strength. SP-based structures can be used under larger loads and have broader application prospects in bearing compressive loads than IWP based structures.

Acknowledgments

The paper was partially funded by the China Scholarship Council. The authors also sincerely thank European Commission for H2020-MSCA-RISE Project No. 691135 "RISEN: Rail Infrastructure Systems Engineering Network," which enables a global research network that tackles the grand challenge in railway infrastructure resilience and advanced sensing under extreme conditions (www.risen2rail.eu)⁶⁰. Technical assistance by John Hammond from Pre-Cast Advanced Track (PCAT) is gratefully acknowledged.

References

1. Gibson, L.J., and Ashby, M.F. (1999) Cellular solids: structure and properties. Cambridge university press.
2. Wu, L., Wang, W., Zhang, W., Su, H., Gu, J., Liu, Q., Zhang, D., Pantelić, D., and Jelenković, B. (2018) Optical Performance Study of Gyroid-Structured TiO₂ Photonic Crystals Replicated from Natural Templates Using a Sol-Gel Method. *Advanced Optical Materials* **6**, 1800064.
3. Saranathan, V., Osuji, C.O., Mochrie, S.G., Noh, H., Narayanan, S., Sandy, A., Dufresne, E.R., and Prum, R.O. (2010) Structure, function, and self-assembly of single network gyroid (I4132) photonic crystals in butterfly wing scales. *Proc Natl Acad Sci U S A* **107**, 11676-11681.
4. Schroder-Turk, G.E., Wickham, S., Averdunk, H., Brink, F., Fitz Gerald, J.D., Poladian, L., Large, M.C., and Hyde, S.T. (2011) The chiral structure of porous chitin within the wing-scales of *Callophrys rubi*. *J Struct Biol* **174**, 290-295.
5. Liu, Y., Schaedler, T.A., Jacobsen, A.J., and Chen, X. (2014) Quasi-static energy absorption of hollow microlattice structures. *Composites Part B: Engineering* **67**, 39-49.
6. Salari-Sharif, L., Schaedler, T.A., and Valdevit, L. (2014) Energy dissipation mechanisms in hollow metallic microlattices. *Journal of Materials Research* **29**, 1755-1770.

7. Melchels, F.P., Bertoldi, K., Gabbriellini, R., Velders, A.H., Feijen, J., and Grijpma, D.W. (2010) Mathematically defined tissue engineering scaffold architectures prepared by stereolithography. *Biomaterials* **31**, 6909-6916.
8. Schaedler, T.A., Ro, C.J., Sorensen, A.E., Eckel, Z., Yang, S.S., Carter, W.B., and Jacobsen, A.J. (2014) Designing Metallic Microlattices for Energy Absorber Applications. *Advanced Engineering Materials* **16**, 276-283.
9. Fu, H., and Kaewunruen, S. (2022) Experimental and DEM investigation of axially-loaded behaviours of IWP-based structures. *International Journal of Mechanical Sciences* **235**, 107738.
10. Ouda, M., Al-Ketan, O., Sreedhar, N., Hasan Ali, M.I., Abu Al-Rub, R.K., Hong, S., and Arafat, H.A. (2020) Novel static mixers based on triply periodic minimal surface (TPMS) architectures. *Journal of Environmental Chemical Engineering* **8**, 104289.
11. Abueidda, D.W., Bakir, M., Abu Al-Rub, R.K., Bergström, J.S., Sobh, N.A., and Jasiuk, I. (2017) Mechanical properties of 3D printed polymeric cellular materials with triply periodic minimal surface architectures. *Materials & Design* **122**, 255-267.
12. Xu, S., Shen, J., Zhou, S., Huang, X., and Xie, Y.M. (2016) Design of lattice structures with controlled anisotropy. *Materials & Design* **93**, 443-447.
13. Afshar, M., Pourkamali Anaraki, A., and Montazerian, H. (2018) Compressive characteristics of radially graded porosity scaffolds architected with minimal surfaces. *Mater Sci Eng C Mater Biol Appl* **92**, 254-267.
14. Hu, Z., Thiagarajan, K., Bhusal, A., Letcher, T., Fan, Q.H., Liu, Q., and Salem, D. (2017) Design of ultra-lightweight and high-strength cellular structural composites inspired by biomimetics. *Composites Part B: Engineering* **121**, 108-121.
15. Sun, G., Jiang, H., Fang, J., Li, G., and Li, Q. (2016) Crashworthiness of vertex based hierarchical honeycombs in out-of-plane impact. *Materials & Design* **110**, 705-719.
16. Zhang, Y., Lu, M., Wang, C.H., Sun, G., and Li, G. (2016) Out-of-plane crashworthiness of bio-inspired self-similar regular hierarchical honeycombs. *Composite Structures* **144**, 1-13.
17. Rashed, M.G., Ashraf, M., Mines, R.A.W., and Hazell, P.J. (2016) Metallic microlattice materials: A current state of the art on manufacturing, mechanical properties and applications. *Materials & Design* **95**, 518-533.
18. Tancogne-Dejean, T., Spierings, A.B., and Mohr, D. (2016) Additively-manufactured metallic micro-lattice materials for high specific energy absorption under static and dynamic loading. *Acta Materialia* **116**, 14-28.
19. Maconachie, T., Leary, M., Lozanovski, B., Zhang, X., Qian, M., Faruque, O., and Brandt, M. (2019) SLM lattice structures: Properties, performance, applications and challenges. *Materials & Design* **183**, 108137.
20. Al-Ketan, O., Adel Assad, M., and Abu Al-Rub, R.K. (2017) Mechanical properties of periodic interpenetrating phase composites with novel architected microstructures. *Composite Structures* **176**, 9-19.
21. Lord, E.A., and Mackay, A.L. (2003) Periodic minimal surfaces of cubic symmetry. *Current Science*, 346-362.
22. Torquato, S., and Donev, A. (2004) Minimal surfaces and multifunctionality. *Proceedings of the Royal Society of London. Series A: Mathematical, Physical and Engineering Sciences* **460**, 1849-1856.
23. Al-Ketan, O., Rowshan, R., and Al-Rub, R.K.A. (2018) Topology-mechanical property relationship of 3D printed strut, skeletal, and sheet based periodic metallic cellular materials. *Additive Manufacturing* **19**, 167-183.

24. Al-Ketan, O., Soliman, A., AlQubaisi, A.M., and Abu Al-Rub, R.K. (2018) Nature-Inspired Lightweight Cellular Co-Continuous Composites with Architected Periodic Gyroidal Structures. *Advanced Engineering Materials* **20**, 1700549.
25. Maskery, I., Sturm, L., Aremu, A.O., Panesar, A., Williams, C.B., Tuck, C.J., Wildman, R.D., Ashcroft, I.A., and Hague, R.J.M. (2018) Insights into the mechanical properties of several triply periodic minimal surface lattice structures made by polymer additive manufacturing. *Polymer* **152**, 62-71.
26. Zhang, L., Feih, S., Daynes, S., Chang, S., Wang, M.Y., Wei, J., and Lu, W.F. (2018) Energy absorption characteristics of metallic triply periodic minimal surface sheet structures under compressive loading. *Additive Manufacturing* **23**, 505-515.
27. Abueidda, D.W., Elhebeary, M., Shiang, C.-S., Pang, S., Abu Al-Rub, R.K., and Jasiuk, I.M. (2019) Mechanical properties of 3D printed polymeric Gyroid cellular structures: Experimental and finite element study. *Materials & Design* **165**, 107597.
28. Al - Ketan, O., Pelanconi, M., Ortona, A., and Abu Al - Rub, R.K. (2019) Additive manufacturing of architected catalytic ceramic substrates based on triply periodic minimal surfaces. *Journal of the American Ceramic Society* **102**, 6176-6193.
29. Yin, H., Liu, Z., Dai, J., Wen, G., and Zhang, C. (2020) Crushing behavior and optimization of sheet-based 3D periodic cellular structures. *Composites Part B: Engineering* **182**, 107565.
30. Jiang, W., Liao, W., Liu, T., Shi, X., Wang, C., Qi, J., Chen, Y., Wang, Z., and Zhang, C. (2021) A voxel-based method of multiscale mechanical property optimization for the design of graded TPMS structures. *Materials & Design* **204**, 109655.
31. Al-Ketan, O., Rowshan, R., Palazotto, A.N., and Abu Al-Rub, R.K. (2019) On Mechanical Properties of Cellular Steel Solids With Shell-Like Periodic Architectures Fabricated by Selective Laser Sintering. *Journal of Engineering Materials and Technology* **141**.
32. Al-Ketan, O., and Abu Al-Rub, R.K. (2019) Multifunctional Mechanical Metamaterials Based on Triply Periodic Minimal Surface Lattices. *Advanced Engineering Materials* **21**, 1900524.
33. Al-Ketan, O., Abu Al-Rub, R.K., and Rowshan, R. (2018) The effect of architecture on the mechanical properties of cellular structures based on the IWP minimal surface. *Journal of Materials Research* **33**, 343-359.
34. Maskery, I., Aboulkhair, N.T., Aremu, A., Tuck, C., and Ashcroft, I. (2017) Compressive failure modes and energy absorption in additively manufactured double gyroid lattices. *Additive Manufacturing* **16**, 24-29.
35. Lee, D.-W., Khan, K.A., and Abu Al-Rub, R.K. (2017) Stiffness and yield strength of architected foams based on the Schwarz Primitive triply periodic minimal surface. *International Journal of Plasticity* **95**, 1-20.
36. Abueidda, D.W., Abu Al-Rub, R.K., Dalaq, A.S., Lee, D.-W., Khan, K.A., and Jasiuk, I. (2016) Effective conductivities and elastic moduli of novel foams with triply periodic minimal surfaces. *Mechanics of Materials* **95**, 102-115.
37. Novak, N., Al-Ketan, O., Krstulović-Opara, L., Rowshan, R., Abu Al-Rub, R.K., Vesenjak, M., and Ren, Z. (2021) Quasi-static and dynamic compressive behaviour of sheet TPMS cellular structures. *Composite Structures* **266**, 113801.
38. Fu, H., and Kaewunruen, S. (2022) State-of-the-Art Review on Additive Manufacturing Technology in Railway Infrastructure Systems. In: *Journal of Composites Science*.
39. Fu, H., Yang, Y., and Kaewunruen, S. (2023) Multi-Hazard Effects of Crosswinds on Cascading Failures of Conventional and Interspersed Railway Tracks Exposed to Ballast Washaway and Moving Train Loads. In: *Sensors*.

40. Li, Y., Li, H., Zhang, G., and Kaewunruen, S. (2023) Nonlinear responses of longitudinally coupled slab tracks exposed to extreme heat waves. *Engineering Structures* **281**, 115789.
41. Ansari, A., Rao, K.S., Jain, A.K., and Ansari, A. (2023) Formulation of multi-hazard damage prediction (MhDP) model for tunnelling projects in earthquake and landslide-prone regions: A novel approach with artificial neural networking (ANN). *Journal of Earth System Science* **132**, 164.
42. Ansari, A., Rao, K.S., and Jain, A.K. (2023) An integrated approach to model seismic loss for the Himalayan infrastructure projects: Decision-making and functionality concept for disaster mitigation. *Bulletin of Engineering Geology and the Environment* **82**, 393.
43. Schwarz, H.J.G.M.A. (1890) Über Minimalflächen. *Monatsber. Berlin Akad.*, April 1865.
44. Schoen, A.H. (1970) Infinite periodic minimal surfaces without self-intersections. *National Aeronautics and Space Administration*.
45. Schwarz, H.A. (1972) *Gesammelte mathematische abhandlungen*. American Mathematical Soc.
46. Fu, H., Huang, X., and Kaewunruen, S. (2023) Experimental investigations into nonlinear dynamic behaviours of triply periodical minimal surface structures. *Composite Structures* **323**, 117510.
47. Yoo, D.-J. (2015) New paradigms in cellular material design and fabrication. *International Journal of Precision Engineering and Manufacturing* **16**, 2577-2589.
48. Houlton, B. (2019) Enhancing packed bed geometry using computational fluid dynamic simulations.
49. Fu, H., Huang, J., and Kaewunruen, S. (2023) Mechanical performance of Bio-Inspired Gyroid and Primitive concrete structures under combined compression and torsion Loads: A discrete element method study. *Engineering Structures* **291**, 116429.
50. Keshavarzan, M., Kadkhodaei, M., Badrossamay, M., and Karamooz Ravari, M.R. (2020) Investigation on the failure mechanism of triply periodic minimal surface cellular structures fabricated by Vat photopolymerization additive manufacturing under compressive loadings. *Mechanics of Materials* **140**, 103150.
51. Brischetto, S., and Torre, R.J.J.o.C.S. (2020) Tensile and Compressive Behavior in the Experimental Tests for PLA Specimens Produced via Fused Deposition Modelling Technique. **4**, 140.
52. Li, Z., Chen, G., Lyu, H., and Ko, F.J.M. (2018) Experimental investigation of compression properties of composites with printed braiding structure. **11**, 1767.
53. Madenci, E., and Guven, I. (2015) *The finite element method and applications in engineering using ANSYS®*. Springer.
54. Chen, X., and Liu, Y. (2018) *Finite element modeling and simulation with ANSYS Workbench*. CRC press.
55. Louche, H., Piette-Coudol, F., Arrieux, R., and Issartel, J. (2009) An experimental and modeling study of the thermomechanical behavior of an ABS polymer structural component during an impact test. *International Journal of Impact Engineering* **36**, 847-861.
56. Dean, G., and Wright, L. (2003) An evaluation of the use of finite element analysis for predicting the deformation of plastics under impact loading. *Polymer Testing* **22**, 625-631.
57. Wang, W., Sun, Y., Lu, Y., Wang, J., Cao, Y., and Zhang, C.J.J.o.t.M.B.o.B.M. (2020) Tensile behavior of bio-inspired hierarchical suture joint with uniform fractal interlocking design. **113**, 104137.

58. Zhang, J., Oueslati, A., Shen, W.Q., and De Saxcé, G. (2019) Shakedown of porous material with Drucker-Prager dilatant matrix under general cyclic loadings. *Composite Structures* **220**, 566-579.
59. Ruiz de Galarreta, S., Jeffers, J.R.T., and Ghouse, S. (2020) A validated finite element analysis procedure for porous structures. *Materials & Design* **189**, 108546.
60. Kaewunruen, S., Sussman, J.M., and Matsumoto, A. (2016) Grand Challenges in Transportation and Transit Systems. *Frontiers in Built Environment* **2**, 4.